Preprint Title	Evaluating analytical performance and characterization of silver-based SERS substrate fabricated by 3D printed microfluidic droplet generation
Authors	Yong-Ill Lee, Phommachith Sonexai, Minh Van Nguyen and Bui The Huy
Publication Date	20 Apr. 2023
Article Type	Full Research Paper
Supporting Information File 1	Supporting information.docx; 2.7 MB
ORCID® iDs	Yong-Ill Lee - https://orcid.org/0000-0001-5383-9801; Minh Van Nguyen - https://orcid.org/0009-0001-5770-0249; Bui The Huy - https://orcid.org/0000-0002-1218-3073

Evaluating analytical performance and characterization of silver-based SERS substrate fabricated by 3D printed microfluidic droplet generation

Phommachith Sonexai, Minh Van Nguyen , Bui The Huy, Yong-Ill Lee*

Anastro Laboratory, Institute of Basic Science, Changwon National University, Changwon 51140, Republic of Korea

_____-

*Corresponding author: Email: yilee@changwon.ac.kr (Y.-I. Lee)

ABSTRACT

The detection of harmful chemicals in the environment and food safety is a crucial requirement. While traditional techniques such as GC-MS and HPLC have provided high sensitivity, they are expensive, time-consuming, and require skilled labor. On the other hand, Surface-enhanced Raman spectroscopy is a powerful analytical tool for detecting ultra-low concentrations of chemical compounds and biomolecules. We present a reproducible method for producing uniform-sized Ag nanoparticles, which can be used to create highly sensitive SERS substrates. A microfluidic device was employed to minimize the precursor reagents within the droplets, resulting in uniform shape and size Ag nanoparticles. The study investigates the effects of various synthesis conditions on the size distribution, dispersity, and localized surface plasmon resonance wavelength of the Ag nanoparticles. To create the SERS substrate, the as-synthesized Ag nanoparticles were assembled into a monolayer on a liquid/air interface and deposited onto a porous silicon array prepared through a metal-assisted chemical etching approach. By using the developed microfluidic, the enhancement factor of the Raman signal for rhodamine B (at 10^{-9} M) and melamine (at 10^{-7} M) was calculated to be 8.59×10^{6} and 8.21×10^{3}, respectively. The detection limits for rhodamine B and melamine were estimated to be 1.94×10^{-10} M and 2.8×10^{-8} M with an RSD ~ 3.4% and 4.6%, respectively. The developed SERS substrate exhibits exceptional analytical performance and has the potential to be a valuable analytical tool for monitoring environmental contaminants.

Keywords: silver nanoparticle; 3D printing; microfluidic droplet; SERS Substrate; smartphone detection.

1. INTRODUCTION

Surface-enhanced Raman spectroscopy (SERS) has emerged as a powerful trace optical detection technique in various biochemical applications due to its exceptional sensitivity, real-time analysis capabilities, and label-free detection [1, 2] and can be used to identify targets for single molecules in chemical and biological systems [3, 4] since the discovery SERS by Martin Fleischmann in 1974 [5]. Electromagnetic and chemical mechanisms are attributed to the SERS enhancement mechanism. In electromagnetic theory, an excitation of light on metal particles leads to the localized surface plasmon resonance due to the collective oscillation of free electrons in the confined space of the metal particles, the electric field is enhanced and the Raman enhancement factor (EF) can reach to 10^6 [6]. The induced amplification of the local field by plasmonic coupling in nano-meter space region around the metal particle is called electromagnetic 'hotspots'. The chemical mechanism suggests the formation of a charge-transfer complex between chemisorbed species and matrix material and gains enhancement when the excitation frequency resonates with a charge-transfer transition [7].

Noble metal nanoparticles (NPs) have gained much popularity in various fields of applications such as analytical chemistry and catalytic chemistry, where they have been used to develop localized surface plasmon resonance (LSPR) and SERS substrates [8]. For example, Ag (NPs) have a stronger SERS effect with cost-effectiveness. However, an issue often encountered in existing synthetic approaches is the non-uniform Ag NPs caused by inhomogeneous mixing conditions. It is crucial to remember that the homogeneity of Ag NPs and their deposition are necessary for the Ag-based SERS substrate to function well. The microfluidic approach is a technique for fine control and manipulation of fluids where capillary penetration is limited to micrometer scale and mass transport dominates [9, 10]. Microfluidic devices are being applied to various fields in industry and laboratories, such as chemical synthesis and micro-reactors [11, 12], drug screening [13], and clinical trials [14]. They can make homogeneous reaction environments with controllable parameters for synthesizing homogeneous colloidal nanoparticles with narrow size distribution [15-17]. Two types of microfluidic devices are commonly used, droplet-based and continuous.

Continuous microfluidic devices have several disadvantages when applied for chemical synthesis purposes, such as laminar flow formation due to the low Reynolds number of fluids, which leads to a lack of uniform mixing [18]. In addition, nanoparticles tend to accumulate on the continued microfluidic channel's sidewall, thus limiting the reuse of the device [8, 19]. On the other hand, droplet-based microfluidic devices are based on the formation of micro-droplets using two or more immiscible fluids with reactants segmented flow and oil continuous flow. They can manage the rate of reactions promoted by mass transfer by convection and diffusion [20, 21]. Furthermore, droplet-based microfluidic devices are frequently utilized to synthesize complex materials of uniform size, as each droplet can function as a separate micro-reactor [12, 22].

A traditional approach to producing microfluidic devices involves a three-step microfabrication process: (i) creating a channel mold using photolithography, (ii) fabrication of the channels by casting the mold through soft lithography, and (iii) bonding channel device to a substrate [23]. This procedure typically requires cleanroom and expensive facilities such as a photolithography machine, spin-coater, and photoresist agents, as well as long processing time and well-trained technical staff. Additionally, the photolithography process is limited to planar fabrication, resulting in low aspect ratio for the achieved features.

Because 3D printing can create and test desired objects in a few hours, providing a new tool for constructing microfluidic devices. This leads to a quick and dynamic process in chemical synthesis and analytical systems at low cost [24-26]. There are two techniques for producing 3D-printed microfluidic devices. In the first approach, monolithic microfluidic devices are 3D-printed devices [27, 28]. Although this one-step process offers the benefits of quick development and ease of fabrication, reducing the channel's dimension to a scale smaller than a millimetre remains challenging [29]. In the second approach, 3D printing can replace photolithography in the conventional microfabrication process to fabricate a mold. This approach can achieve a better lateral resolution of printed features down to 100 μm with a higher aspect ratio of the printed channel feature [30], and does not require a cleanroom. Stereo-lithography (SLA) technique operates based on an

additive manufacturing technique in which a photopolymer resin is cured and converted from liquid to solid state by an ultraviolet laser. The resolution of SLA printers is determined by radial beam scattering and the types of resin [31]. With particular resins, SLA can fabricate features with a lateral dimension of 100 µm and a mold-printed resolution of 50 µm.

Over the past decade, numerous SERS substrates based on various materials, including paper [32, 33], polymers [34, 35], fibers [36], dielectrics [37], porous aluminum oxide [38], and semiconductors [39] have been reported. Dielectric and semiconductor substrates have been particular popular due to their larger contribution to the amplification of the Raman signal and longer shelf life, such as ZnO nanowires, silicon nanowires, and porous silicon (PS) [40-42]. Silicon nanostructures with high specific areas are especially popular because they have no fluorescence properties.

In this work, we report the highly sensitive SERS substrate for detecting Rhodamine B (RhB) and Melamine (MLM) with assessing the applicable analytical propertyof the developed systemThe substrate was prepared from Ag NPs by decorating the surface of porous silicon with Ag NPs. The Ag NPs were synthesized using a droplet-based microfluidic device and an Stereolithographic (SLA) 3D printing method. The microfluidic device was optimized to produce uniform droplets, within which silver nitrate was reduced by sodium borohydride. This method limited the amount of precursors chemicals used and enabled the sequential flow of droplets, resulting in silver nanoparticles of uniform shape and size. We investigated the effects of different synthesis conditions on size distribution, dispersity, and LSPR wavelength of the silver nanoparticles.

2. EXPERIMENTAL PROCEDURE

2.1. Chemicals and apparatus

Silver nitrate ($AgNO_3$, 99.9%) was purchased from Kojima chemical (Japan)., Sodium borohydride ($NaBH_4$, 98%), and melamine (99%) were obtained from Sigma-Aldrich (Republic of Korea). Hydrofluoric acid (48-51%), sulfuric acid (98%), nitric acid (65-70%), Rhodamine B (pure), mineral oil (light molecular biology grade), sorbitan monooleate (SPAN 80), and trisodium citrate dehydrate (TCD) (99%) were purchased

from Alfa Aesar (Republic of Korea). Sylgard 184 A&B was obtained from Sewang Hitech (Republic of Korea), and the XL-1500 UV Cross-linker used for UV curing was purchased from Krackeler Scientific (USA). Methyl alcohol, hydrogen peroxide (35%), sodium hydroxide (<97%), ammonia water (25-29%), acetone (99.5%), ethyl Alcohol (95%), 2-propanol (99.5%) were bought from Daejung (Republic of Korea). The Formlabs 3D printer and clear V4 resin were purchased from Formlabs (USA). Deionized water with a resistivity of 18 $M\Omega.cm^{-1}$, provided by a Milli-Q water purification system (Millipore Corp., MA, USA), was used throughout all the experiments.

The morphology of Ag NPs and SERS substrates were examined using the field emission scanning electron microscope (FE-SEM, Mira II, TESCAN). The UV/VIS spectrometer (Agilent 8453, Agilent, USA) and Micro-Raman (NS200, Nanoscope system, Republic of Korea) were used to record the absorption spectra and Raman spectra, respectively.

2.2. Fabrication of droplet-based microfluidic device

The fabrication process of a microfluidic device is illustrated in **Scheme S1,** in Supporting file. The 3D model of the microfluidic device mold was designed precisely by Solidworks Professional 2022 SP3.1 software and printed on the Formslab 3 SLA 3D printer (Formlabs Inc., Somerville, MA, USA)) using Clear V4 resin. The mold underwent post-treatment by being soaked for 20 minutes in a 90% (v/v) isopropanol solution, followed by 10 minutes in deionizedwater, and then gently dried with a nitrogen flow. After that, the molds were exposed to UV light at an energy level of 120 mJ/cm^2 for 30 seconds and then annealed at 60 °C for 12 hours in an oven for slow evaporative drying (**Scheme S1a)**. Before casting into the printed mold, Polydimethylsiloxane (PDMS) Sylgard^{TM} 184, and curing agent (10:1, w:w) were mixed for ten minutes and de-bubbled under a vacuum for 30 min. The PDMS-casted mold was dried for 18 hours to cure it after being dried in the air for 24 h (**Scheme S1b)**. The PDMS was peeled off from the mold, and it was then given a 24 h immersion in a 1M NaOH solution (**Scheme S1c)**. Finally, the PDMS was carefully adhered to the surface of the glass plate **(Scheme S1d)** and treated at

90 °C for 5 min on a hot plate. Following this step, silicon tubes were joined to the inlets of the microfluidic device using Loctite superglue.

2.3. Synthesis of silver nanoparticles using the droplet-based microfluidic device

The droplet-based microfluidic device was used to synthesize Ag NPs. These droplets enable the uniform distribution of nanoparticles. Ag NPs were created by reducing $AgNO_3$ solutions with $NaBH_4$ as a reducing agent and TCD as a stabilizer [43, 44]. The mineral oil serves as a continuous phase when combined with the surfactant Span 80 (2% w/v). To prevent droplets from coalescing in the microchannel, Span 80 was added to lower the interfacial tension between the oil and aqueous phases.

For the syhthesis of Ag NPs, 20 mL of $AgNO_3$ and 20 mL of TSC were mixed to form the reactant solution in 1:3 molar ratios, assigned as a solution (a); 20 mL of $NaBH_4$ and NaOH were mixed in a 1:3 molar ratio, assigned as a solution (b). Two syringe pumps were used to inject the mineral oil mixed with the surfactant Span 80 (2% w/v), solution (a), and (b) into the droplet-based microfluidic system at a flow rate of 20:80 µL/min.

The as-synthesized colloidal solution of Ag NPs was centrifuged at 12,000 rpm for 5 min to separate the Ag NPs solution and remove the oil phase. Finally, the Ag NPs suspension was stored in a dark vial at room temperature for further experiments.

2.4. Fabrication of porous silicon (PS) substrate

A wafer with the p-type Si (100) and a resistivity of 0.01–0.09 Ω cm was used in this word. The wafers were divided into 1×1 cm^2 and then cleaned with an ultrasonic cleaner in acetone (20 min), ethanol (15 min), and deionized water (10 min). The pieces of wafers were oxidized in hot Piranha (45 mL of H_2SO_4: 15 mL of H_2O_2) for 5 min. To perform metal-assisted chemical etching (MACE), the wafers were placed in a beaker containing an etchant solution made up of 5 mL of HF 4.6M and 5 mL of $AgNO_3$ 0.02M. The etching timings were 0, 5, 10, 20, 40, and 80 min. After the etching process to remove the as-generated Ag dendrites, the substrates were immediately submerged in concentrated HNO_3, rinsed with deionized water, and then dried at room temperature to produce a PS substrate.

2.5. Fabrication of SERS substrate

The colloidal Ag NPs solutions were generated at the methanol/air interface by adapting the method described in the previous report [45]. Briefly, 5 mL of the colloidal solution of Ag NPs and 5 mL of acetone were mixed in a 50 mL glass vial. This mixture was quickly poured into another glass vial containing 5 mL of hexane. The vial was shaken for 30 seconds, and then stabilized for 10 minutes, the Ag NPs moved from the water into the hexane with the aid of acetone. The porous silicon (PS) template substrate was placed at the bottom of a beaker containing methanol. A pipette was then used to gradually transfer the Ag NPs suspension in hexane to the surface of methanol. After the hexane evaporated, a tightly packed monolayer of Ag NPs appeared at the methanol/air interface. The PS@Ag substrates were created by depositing a monolayer of Ag NPs on the substrate's surface after allowing the methanol to slowly evaporate under ambient conditions.

2.6. SERS substrate characterization

Raman spectra were obtained using a 24 mW laser and an integration time of 1000 ms. Asymmetric least-squares baseline subtraction was utilized to remove the SERS spectrum background. Each Raman spectrum represents the mean of three readings. Aqueous solutions of RhB and MLM were prepared at varying concentrations, and the SERS substrate was loaded with the analyte solution (30 µL) and air-dried at room temperature. SERS signals were then collected from random locations.

3. RESULTS AND DISCUSSION

3.1. Fabrication of droplet-based microfluidic device using 3D printing

SLA 3D printing is an additive manufacturing technology that employs a laser to transform liquid resin into a solid plastic. When exposed to laser radiation with an appropriate wavelength, the short molecular chains in photocurable resins form chains, resulting in the polymerization of monomers and oligomers into rigid or flexible geometries that solidify. As the printing limit of the 3D line dimension suggested by the Formlabs 3 printer manufacturer is 100 µm × 100 µm, a mold with line features was created instead of printing the microfluidic device directly. To minimize defects during the

printing of the mold, the micro-channel was designed with larger dimensions. Three inlets for the mixing channel were made with a width and depth of 200 µm × 150 µm, respectively, while the mixing channel had dimensions of 400 µm × 200 µm. The total length of the serpentine-shaped micro-channel, which is the reaction length, was 605.6 mm, as shown in Figure S1. The photograph of the microfluidic device that was prepared is illustrated in Figure 1. The droplet-based microfluidic device was constructed with three inlets for introducing reactants and oil, a long serpentine-shaped micro-channel for combining chemical solutions, and one outlet for collecting suspended Ag NPs.

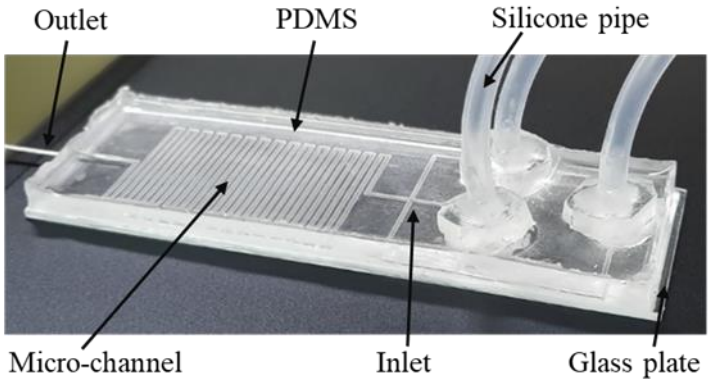

Figure 1: Photograph of the as-fabricated droplet-based microfluidic device.

The PDMS was bound with a glass plate after peeling off from the mold. There are various surface treatment methods available, including oxygen plasma, UV/ozone, corona oxidizer, and plasma pen [46, 47]. In this study, we employed a chemical treatment method that uses a NaOH 1M solution for 24 hours, which was previously reported [48]. Chemical treatment was also applied to the glass plate as the silicon substrate. Although this method takes longer, it is more cost-effective, straightforward, and accessible. The aforementioned chemical treatment of PDMS and the glass plate aims to decorate their surfaces with silanol groups (Si-OH), enabling two surfaces to bond chemically at the atomic level [49]. To determine the droplet size, we used two dye solutions and captured images of the observed droplets (Figure S2). The Supporting information file contains data on the flow rate of the aqueous solution to oil and the droplet size (Figures S3-S7). Our investigation revealed that the optimal flow rate is 20:80 µL/min.

3.2. Synthesis of silver nanoparticles via droplet-based microfluidic device

Various mole ratios of silver nitrate to sodium borohydride were used to produce Ag nanoparticles in a microfluidic device at room temperature, with a flow rate ratio of 20:80 µL/m for aqueous solutions to oil, as described in detail in the Supporting Information. The use of high concentrations of $AgNO_3$ resulted in the formation of numerous Ag nuclei due to a rapid reduction process. The collision frequency of these nuclei with a higher concentration of silver nitrate increases significantly, promoting the formation of larger particles from smaller ones. This phenomenon explains the observed color change from yellow to greenish after three weeks, as illustrated in Figure S8 [50, 51]. $NaBH_4$ is a relatively potent reducing agent that can reduce Ag^+. At higher concentrations of $NaBH_4$, the formation of silver nanoparticles occurs more rapidly [52]. When the concentrations of silver nitrate and trisodium citrate were kept constant, and the concentration of sodium borohydride was varied from 5-20 mmol, the capping agent decreased, resulting in a change in the color of the obtained solution from yellowish to bright yellow after three weeks, as shown in Figure S9. The Ag nanoparticles remained almost unchanged after three weeks when the ratio of silver nitrate to sodium borohydride was kept constant, especially with a molar ratio of 10:10 (in mM), as demonstrated in Figure 2.

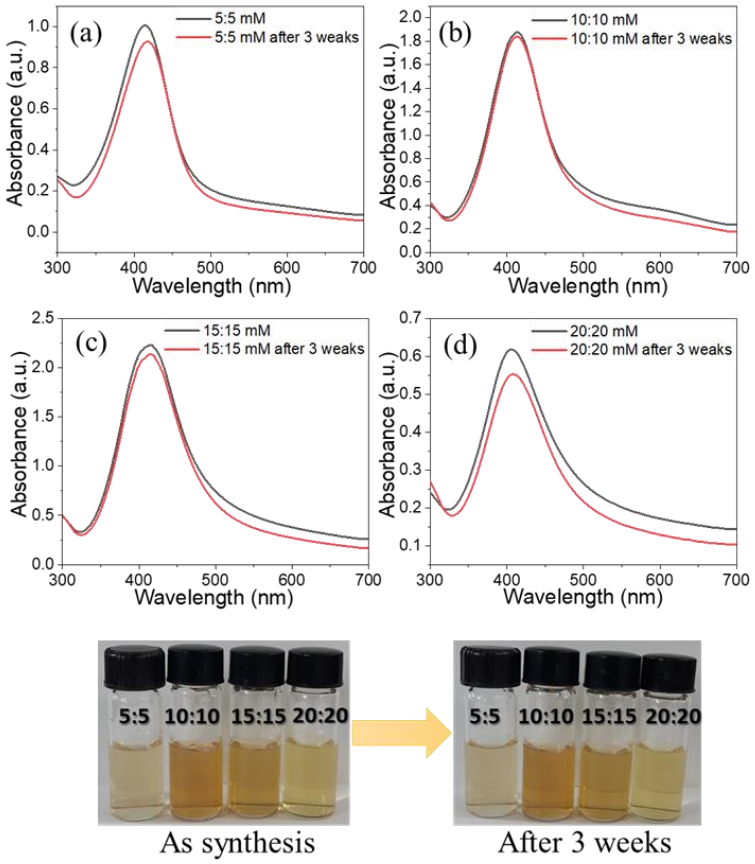

Figure 2. Images and absorbance spectra of Ag NPs synthesized using silver nitrate and sodium borohydride with the ratios of 5:5 (a), 10:10 (b), 15:15 (c), and 20:20 (d) (in mM).

FE-SEM micrographs of the samples are shown in Figure 3. The average sizes of Ag nanoparticles were estimated to be 24.10 ± 0.15 nm, 27.07 ± 0.16 nm, 28.07 ± 0.17 nm, and 30.88 ± 0.31 nm by using ImageJ program. Based on the calculated data, it is evident that the average size of Ag NPs increases with an increase in the concentration of reactants.

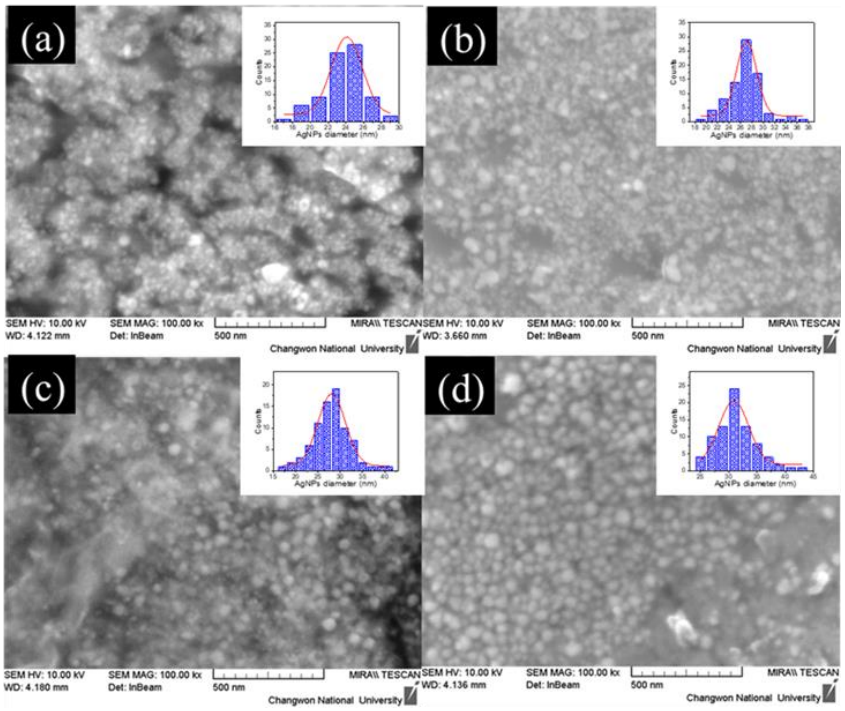

Figure 3. FE-SEM images of the synthesized Ag NPs with the molar ratios of silver nitrate and sodium borohydride to be of 1:1 mM (a), 5:5 mM (b), 10:10 mM (c), and 15:15 mM (d) samples. Insets of the figures are size distributions drawn by ImageJ software.

3.3. Structural characterization of the SERS substrate

Figure S10a shows the SEM image of the self-assembled monolayer (SAM) of Ag NPs on the surface of methanol, while Figure S10b displays the image of the PS-deposited wafer after covering Ag NPs. The SEM image of PS@Ag reveals the presence of nano-gaps between the Ag NPs, which act as "hot spots" with a high electric field intensity when exposed to laser irradiation (Figure S10c). To confirm the distribution of chemical elements on the SERS substrate, an energy dispersion spectrum (EDS) was acquired, as illustrated in Figure S11. The EDS mapping results indicate that the element silicon is uniformly distributed on the SERS substrate. The silicon peak has the highest intensity due to the presence of a silicon wafer, while oxygen and silver are discontinuously distributed owing to the space between the PS and Ag NPs on the PS@Ag substrate.

3.3.1. Optimizing the fabrication process of PS@Ag SERS substrate

To optimize the etching time of PS on the wafers, the RhB solution (10^{-5} M) was chosen for estimating the SERS signal. The wafer pieces are etched for 0, 5, 10, 20, 40, and 80 min. These substrates are assigned as PS0min@Ag, PS5min@Ag, PS10min@Ag, PS20min@Ag, PS40min@Ag, and PS80min@Ag. The SEM images revealed that the SAM of Ag NPs on the substrate without etching is not uniform, as shown in Figure S12. Meanwhile, the substrates with etching times of 5 min, and 10 min, their SAM illustrated some islands that were not continuous as shown in Figure S12b-c. By extending the etching time from 20 min to 80 min, especially with an etching period of 40 min, as shown in Figure S12d-f, the silver nanoparticles were well ordered.

Figure 4a shows the SERS spectra of RhB on substrates with varied etching times. The spectra exhibit peaks at 621, 1199, 1279, 1358, 1508, 1528, and 1647 cm^{-1}. The peaks at 621, 1199, and 1279 cm^{-1} are associated with the deformation vibration of the xanthene ring, the stretching of the C─C bridge-bands, and the bending of the aromatic C─H, respectively. The peaks at 1358, 1508, and 1528 cm^{-1} are linked to the aromatic C─C bending, while the peak at 1647 cm^{-1} is determined by the bending and stretching of the C─C bonds [53].

The SERS intensity increases with an extension of the etching time of the PS substrate from 0 min to 40 min, and it decreases quickly with a longer etching time. This may be due to the development of deeper and larger pores on the PS surface. The intensities of the peaks from the sample PS0min@Ag are significantly lower than those of the other samples. In comparison with the PS40min@Ag sample, the intensity of the peak at 621 cm^{-1} is approximately sixty times lower (Figure 4b). This confirms that the etching time of PS is a critical parameter for the fabrication of the SERS substrate. The substrate with an etching time of 40 min (PS40min@Ag) exhibits the best SERS performance and thus was chosen as the optimal substrate for future tests.

The influence of the Ag NPs sizes on the SERS signals was studied. Four different sizes of Ag NPs (24 nm, 27 nm, 28 nm, and 30 nm) were self-assembled on the PS40min@Ag substrate. The SERS spectra of RhB (10^{-5} M) were collected using each size of Ag NPs, as shown in Figure 4c. A slight increase in intensity was observed as the diameter of Ag NPs increased from 24 nm to 30 nm (Figure 4d). Based on these findings, we selected Ag NPs with

a diameter of 28 nm as the optimal choice for the SERS substrate and used them for further experiments.

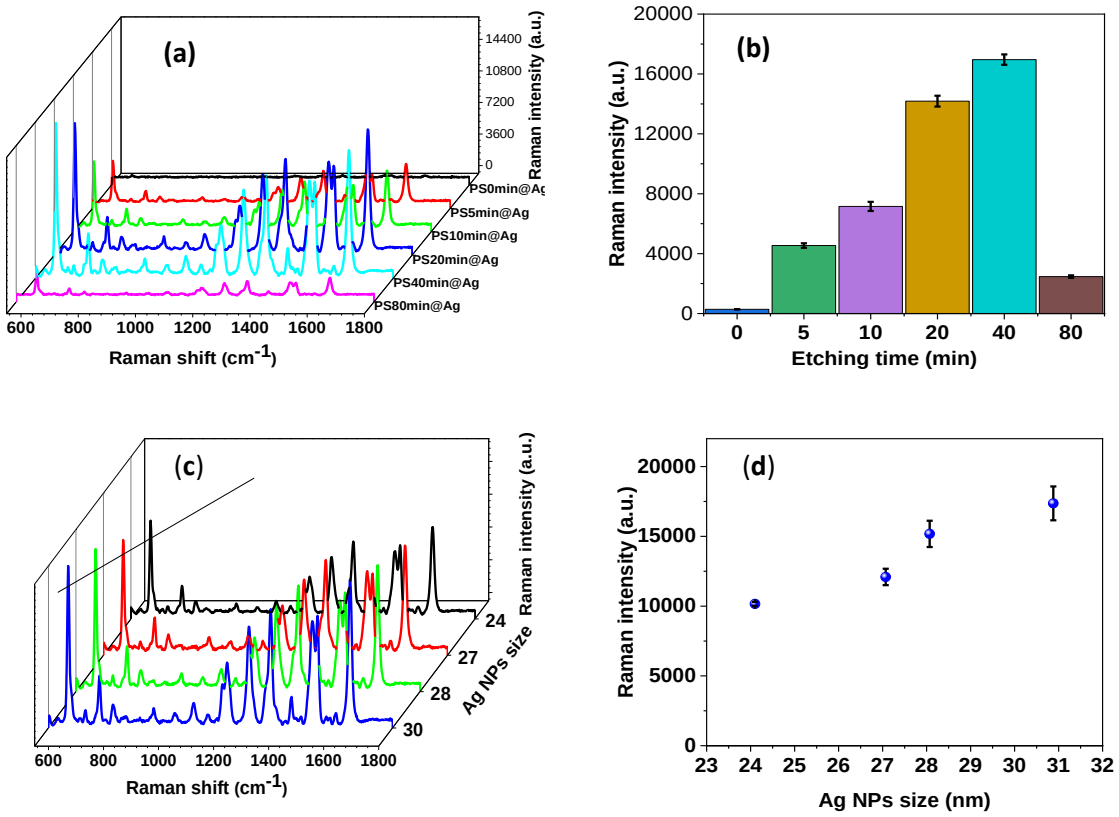

Figure 4. (a) SERS spectra based on etching time of PS, (b) Intensity of 621 cm^{-1} SERS with the different etching times, (c) SERS spectra of RhB based on Ag NPs different diameters on the PS40min@Ag substrate, (d) Intensity of the SERS peak at 621cm^{-1} using different sizes of Ag NPs.

3.3.2. Relationship between RhB's concentration and Raman intensity

The SERS spectra of RhB samples were collected using the PS40min@Ag substrate at various concentrations, ranging from 10^{-9} M to 10^{-5} M, as presented in Figure 5a. The SERS intensity of RhB increased as the concentration increased. Figure 5b illustrates the correlation between RhB concentration and the peak intensity at 621 cm^{-1}, which was used to create a linear calibration line with a high regression coefficient of $R^2 = 0.99968$. By applying the $3\sigma/s$ method, where σ is the standard deviation of the blank and s is the slope of the linear regression

equation, the limit of detection was found to be 1.94×10^{-10} M. The SERS substrates showed an enhancement factor (EF) of 8.59×10^{6} at the 621 cm^{-1} peak with an RhB concentration of 10^{-9} M. The calculation details for the EF can be found in the "Enhancement factor calculation" section of the Supporting Information file.

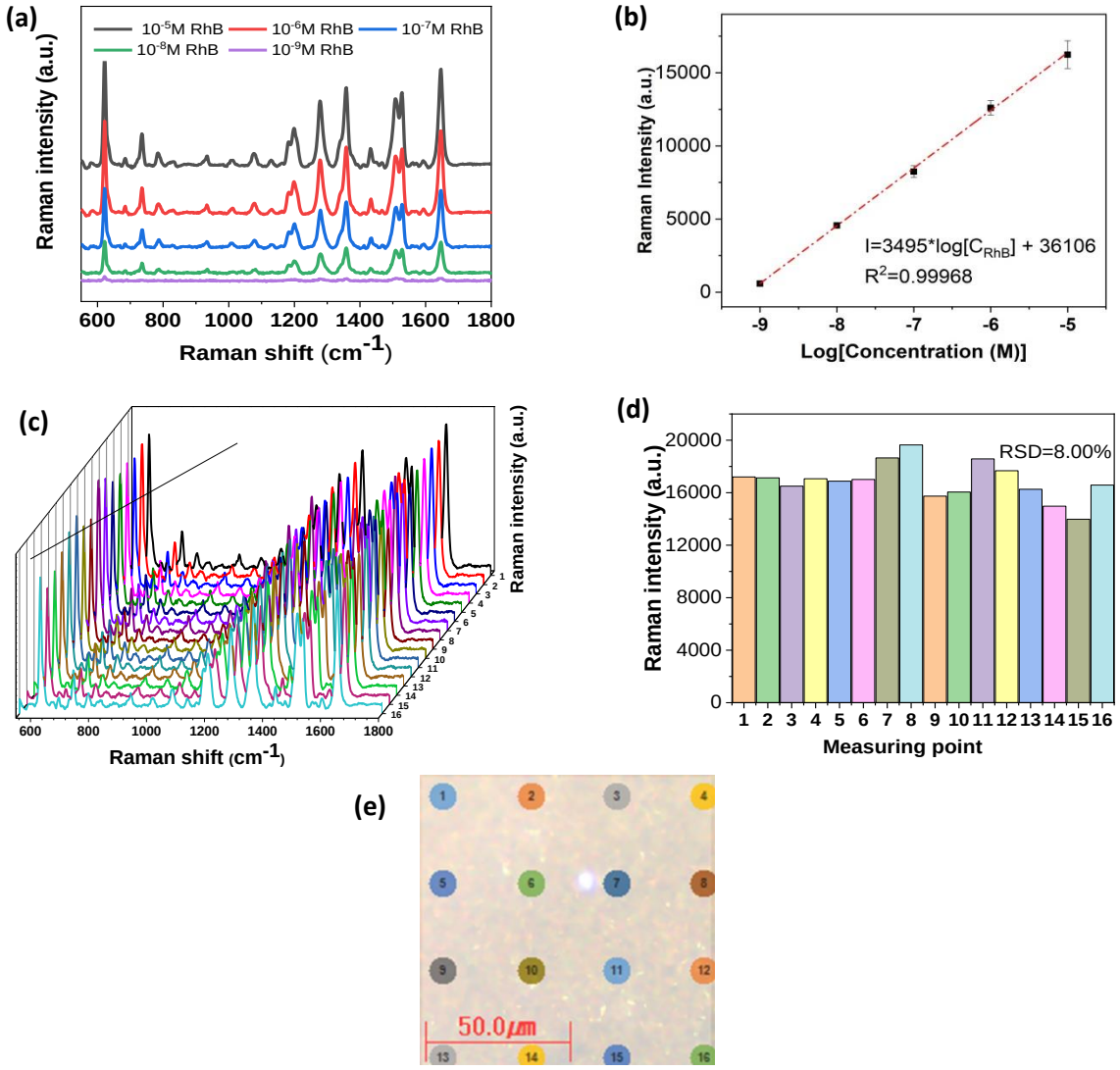

Figure 5. (a) Raman spectra of RhB solution in the range of 10^{-9} - 10^{-5} M, (b) Dependence of Raman intensity on RhB concentrations at peak 621 cm^{-1}, (c) SERS spectra and (d) SERS intensity at peak 621 cm^{-1} when mapping the SERS substrate at 16 positions, and (e) Surface area of the mapping measurement.

To investigate the uniformity of the SERS substrate, Raman mapping was performed on an area of 100 µm × 100 µm with 16 measuring positions. RhB with a concentration of 10^{-5} M was introduced to the PS40min@Ag substrate. Figure 5c displays the SERS spectra collected from each position, while Figure 5d shows the SERS peak at 621 cm-1 for the different positions. The relative standard deviation (RSD) was calculated to be 8%, indicating that the PS@Ag structure was homogeneously prepared due to the even deposition of the self-assembled monolayer of Ag NPs on the PS.

3.4. Detection of melamine using PS@Ag SERS substrate

The SERS spectra of MLM solutions at various concentrations (10^{-7} - 10^{-3} M) on the PS@Ag substrates were recorded to examine the prepared SERS substrate, as shown in Figure 6a. The Raman spectra of MLM consisted of peaks at 585, 679, and 985 cm^{-1}. The peak at 583 cm^{-1} is related to the mixed mode of N─C─N bending and NH_2 twisting vibration, 679 cm^{-1} is attributed to the plane deformation modes of the triazine ring, and 985 cm^{-1} is ascribed to ─CN vibration [54].

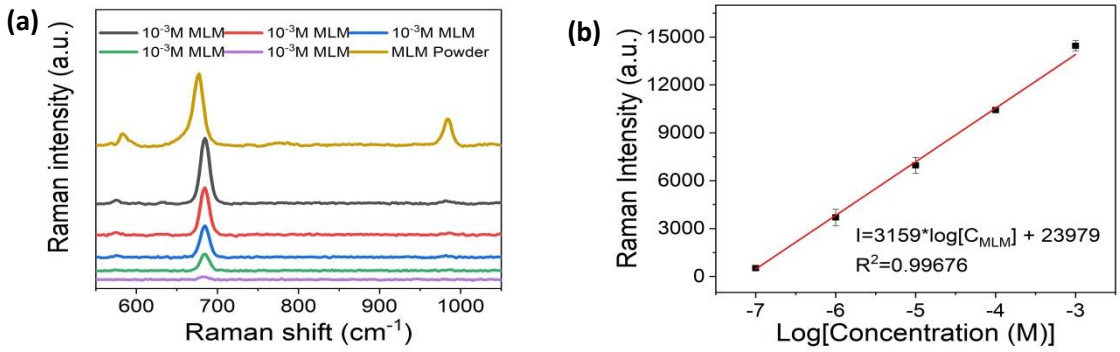

Figure 6. (a) Raman spectra of powder and trace concentrations of MLM (10^{-7} - 10^{-3} mol/L), (b) Dependence of SERS intensity on MLM concentration at the 682 cm^{-1} peak.

The relationship between SERS intensity at the fingerprint peak of 682 cm^{-1} and MLM concentration is displayed in Figure 6b. The calculated limit of detection for MLM was found to be 2.8 × 10^{-8} M, which is significantly below the safety limit established by the US Food and Drug Administration[55]. The SERS substrates displayed an impressive EF of 8.21 × 10^{3} at the 682 cm^{-1} peak with an MLM concentration of 10^{-7} M, indicating excellent SERS

performance of the prepared. Further information on the calculation of the EF can be accessed in the "Enhancement factor calculation" section of the Supporting Information file.

4. CONCLUSION

Using 3D printing, a droplet-based microfluidic device was successfully fabricated without the need for expensive and time-consuming photolithography. The resulting devices were utilized to produce uniformly distributed silver nanoparticles that were then applied to the surface of a porous silicon substrate via a novel self-assembly technique. This created a SERS substrate, which was able to detect RhB and MLM, with detection limits of 1.94×10^{-10} M and 2.8×10^{-8} M, respectively. Enhancement factors of 8.59×10^{6} and 8.21×10^{3} were achieved for RhB and MLM, respectively. SERS mapping showed the substrate to have good homogeneity with an RSD of 8%. These results demonstrate the excellent analytical performance of the PS@Ag SERS substrate, making it a promising tool for detecting environmental pollutants and ensuring food safety

ACKNOWLEDGMENTS

This work was supported by the National Research Foundation of Korea (NRF) grant funded by the Korea government (MSIT) (NRF-2023R1A2C1004414).

REFERENCES

[1] Fan, M.; Andrade, G.F.S.; Brolo, A.G. Anal Chim Acta. **2020**, 1097, 1-29.

[2] Langer, J., et al. ACS Nano. **2020**, 14, 28-117.

[3] Almehmadi, L.M., et al. Sci Rep. **2019**, 9, 12356.

[4] Keshavarz, M.; Kassanos, P.; Tan, B.; Venkatakrishnan, K. Nanoscale Horizons. **2020**, 5, 294-307.

[5] Fleischmann, M.; Hendra, P.J.; McQuillan, A.J. Chemical Physics Letters. **1974**, 26, 163-166.

[6] McCall, S.L.; Platzman, P.M.; Wolff, P.A. Physics Letters. **1980**, 77, 381-383.

[7] Strommen, D.P.; Nakamoto, K. Chemical Education. **1977**, 54, 474.

[8] Nie, Y.; Jin, C.; Zhang, J.X.J. ACS Sens. **2021**, 6, 2584-2592.

[9] Kuo, J.S.; Chiu, D.T. Annu Rev Anal Chem (Palo Alto Calif). **2011**, 4, 275-296.

[10] Zhao, C.-X.; He, L.; Qiao, S.Z.; Middelberg, A.P.J. Chemical Engineering Science. **2011**, 66, 1463-1479.

[11] Elvira, K.S.; Casadevall i Solvas, X.; Wootton, R.C.; deMello, A.J. Nat Chem. **2013**, 5, 905-915.

[12] Abalde-Cela, S.; Taladriz-Blanco, P.; de Oliveira, M.G.; Abell, C. Sci Rep. **2018**, 8, 2440.

[13] Kwapiszewska, K., et al. Lab Chip. **2014**, 14, 2096-2104.

[14] Iyer, V., et al. Lab on a Chip. **2022**, 22, 3110-3121.

[15] Wang, J., et al. Lab Chip. **2017**, 17, 1970-1979.

[16] Thu, V.T., et al. Journal of Electronic Materials. **2016**, 45, 2576-2581.

[17] Choi, J.W., et al. BioChip Journal. **2020**, 14, 298-307.

[18] Xia, H.M.; Wan, S.Y.; Shu, C.; Chew, Y.T. Lab Chip. **2005**, 5, 748-755.

[19] Hohn, E.M.; Panneerselvam, R.; Das, A.; Belder, D. Anal Chem. **2019**, 91, 9844-9851.

[20] Wang, J., et al. Micromachines. **2017**, 8,

[21] Sahin, S.; Bliznyuk, O.; Rovalino Cordova, A.; Schroen, K. Sci Rep. **2016**, 6, 26407.

[22] Cheng, Y., et al. Nanoscale Adv. **2021**, 3, 2180-2195.

[23] Damodara, S., et al. Materials and methods for microfabrication of microfluidic devices. in Microfluidic Devices for Biomedical Applications (Second Edition) Woodhead Publishing, 2021, pp. 1-78.

[24] Li, Y., et al. Int J Pharm. **2020**, 583, 119388.

[25] Duarte, L.C., et al. Anal Chim Acta. **2022**, 1190, 339252.

[26] Bressan, L.P., et al. Microchemical Journal. **2019**, 146, 1083-1089.

[27] Xu, Q.; Lo, J.; Lee, S.-W. Applied Sciences. **2020**, 10,

[28] Litti, L.; Trivini, S.; Ferraro, D.; Reguera, J. ACS Appl Mater Interfaces. **2021**, 13, 34752-34761.

[29] Wang, L.; Pumera, M. TrAC Trends in Analytical Chemistry. **2021**, 135, 116151.

[30] Mohamed, M., et al. Journal of Manufacturing and Materials Processing. **2019**, 3, 26.

[31] Gross, B.C., et al. Anal Chem. **2014**, 86, 3240-3253.

[32] Thuy, T.T., et al. Nano Select. **2020**, 1, 499-509.

[33] Lin, S., et al. Anal Methods. **2020**, 12, 2571-2579.

[34] Xing, L., et al. ACS Appl Mater Interfaces. **2022**, 14, 13480-13489.

[35] Yang, N., et al. J Agric Food Chem. **2018**, 66, 6889-6896.

[36] Ge, F., et al. Cellulose. **2019**, 26, 2689-2697.

[37] Shanthil, M.; Fathima, H.; George Thomas, K. ACS Appl Mater Interfaces. **2017**, 9, 19470-19477.

[38] Chen, J., et al. J Food Sci. **2015**, 80, N834-840.

[39] Zhang, C., et al. Opt Express. **2015**, 23, 24811-24821.

[40] Kara, S.A., et al. RSC Advances. **2016**, 6, 93649-93659.

[41] Rani, S.; Shukla, A.K. Thin Solid Films. **2021**, 723, 138595.

[42] Lai, Y.-C., et al. Applied Surface Science. **2018**, 439, 852-858.

[43] Hao, N.; Nie, Y.; Xu, Z.; Zhang, J.X.J. J Colloid Interface Sci. **2019**, 542, 370-378.

[44] Sarjuna, K. The Electrochemical Society. **2022**, 107, 4113.

[45] Leiterer, C., et al. Journal of Nanoparticle Research. **2014**, 16, 2467.

[46] Solis-Tinoco, V.; Marquez, S.; Sepulveda, B.; Lechuga, L.M. RSC Advances. **2016**, 6, 85666-85674.

[47] Natarajan, S.; Chang-Yen, D.A.; Gale, B.K. Journal of Micromechanics and Microengineering. **2008**, 18, 045021.

[48] Hoek, I.; Tho, F.; Arnold, W.M. Lab Chip. **2010**, 10, 2283-2285.

[49] Maji, D.; Lahiri, S.K.; Das, S. Surface and Interface Analysis. **2012**, 44, 62-69.

[50] Sobczak-Kupiec, A.; Malina, D.; Wzorek, Z.; Zimowska, M. Micro & Nano Letters. **2011**, 6, 656.

[51] Fu, L.M., et al. Micromachines (Basel). **2021**, 12, 1123.

[52] Zhang, Q., et al. J Am Chem Soc. **2011**, 133, 18931-18939.

[53] Sun, Y., et al. Food Chem. **2021**, 357, 129741.

[54] Huy, B.T., et al. Journal of Luminescence. **2017**, 188, 436-440.

[55] Dao, D.Q., et al. J Phys Chem A. **2021**, 125, 8529-8541.